RESEARCH ARTICLE

An nMgO containing scaffold: Antibacterial activity, degradation properties and cell responses

Cijun Shuai[1,2,3], Wang Guo[1], Chengde Gao[1], Youwen Yang[1], Ping Wu[4] and Pei Feng[1*]

[1] State Key Laboratory of High Performance Complex Manufacturing, College of Mechanical and Electrical Engineering, Central South University, Changsha, China
[2] Jiangxi University of Science and Technology, Ganzhou, China
[3] Key Laboratory of Organ Injury, Aging and Regenerative Medicine of Hunan Province, Changsha, China
[4] College of Chemistry, Xiangtan University, Xiangtan, China

Abstract: Bone repair failure caused by implant-related infections is a common and troublesome problem. In this study, an antibacterial scaffold was developed via selective laser sintering with incorporating nano magnesium oxide (nMgO) to poly(3-hydroxybutyrate-co-3-hydroxyvalerate) (PHBV). The results indicated the scaffold exerted high antibacterial activity. The antibacterial mechanism was that nMgO could cause oxidative damage and mechanical damage to bacteria through the production of reactive oxygen species (ROS) and direct contact action, respectively, which resulted in the damage of their structures and functions. Besides, nMgO significantly increased the compressive properties of the scaffold including strength and modulus, due to its excellent mechanical properties and uniform dispersion in the PHBV matrix. Moreover, the degradation tests indicated nMgO neutralized the acid degradation products of PHBV and benefited the degradation of the scaffold. The cell culture demonstrated that nMgO promoted the cellular adhesion and proliferation, as well as osteogenic differentiation. The present work may open the door to exploring nMgO as a promising antibacterial material for tissue engineering.

Keywords: Nano magnesium oxide; antibacterial scaffolds; degradation properties; cytocompatibility; mechanical properties

*Correspondence to: Pei Feng, State Key Laboratory of High Performance Complex Manufacturing, College of Mechanical and Electrical Engineering, Central South University, Changsha, 410083, China; fengpei@csu.edu.cn

Received: September 17, 2017; **Accepted**: October 10, 2017; **Published Online**: November 1, 2017

Citation: Shuai C, Guo W, Gao C, *et al.*, 2018, An nMgO containing scaffold: Antibacterial activity, degradation properties and cell responses. *Int J Bioprint*, 4(1): 120. http://dx.doi.org/10.18063/IJB.v4i1.120

1. Introduction

Bone scaffolds are usually susceptible to bacterial infections, which easily result in the failure of bone repair[1–3]. In clinic, administration of antibiotics is a frequently used method for prophylaxis and treatment of infections. However, long-term administration of antibiotics easily causes toxic and adverse effects to the human body such as hypersensitivity and immunosuppression; and the abuse of antibiotics has given rise to serious multiple drug resistance of many pathogenic bacteria[4–7]. Therefore, it is extremely necessary to explore new methods of dealing with the implant-related bacterial infections.

Developing antibacterial scaffolds may be a promising strategy with incorporating antibacterial materials[8–10]. Metallic oxides, including silver oxide, copper oxide, titanium dioxide and magnesium oxide (MgO), have attracted attention owing to their high antibacterial activity and broad antibacterial spectrum[11–13]. Among them, MgO, and especially nanosized MgO (nMgO), is more promising, considering that it has not only strong antibacterial activity but also excellent biocompatibility, which has been recognized as safe by the US Food and Drug Administration (21CFR184.1431)[14]. Besides, its alkaline degradation products may be in favor of constructing weakly alkaline microenvironments for cellular responses; the magnesium ion is widely involved in human metabolisms, playing an significant role in regulating cellular responses[15]. In addition, it has been previously used as a rigid filler for reinforcing polymer[16,17].

Haldorai and Shim[18] prepared chitosan/MgO composites by chemical precipitation method and found the composites showed a much higher killing rate against

Escherichia coli (*E. coli)* compared with chitosan. Yamamoto *et al*.[19] prepared calcium carbonate/nMgO composites *via* thermal decomposition of dolomite and found the composites exerted high antibacterial properties towards *E. coli* and *Staphylococcus aureus*. Ma *et al*.[20] prepared poly(L-lactide)/nMgO composites and found nMgO neutralized the acidic degradation products of poly(L-lactide) and improved its mechanical properties. Nevertheless, studies on MgO-containing composites for biomedical applications are still very lacking, and few papers, to the best of our knowledge, have systematically studied their comprehensive performances, especially in the form of scaffolds.

In this study, nMgO was incorporated to PHBV for developing antibacterial bone scaffolds. Three-dimensional porous PHBV/nMgO scaffolds were prepared by selective laser sintering (SLS). The antibacterial activity of the scaffolds was evaluated, while the antibacterial mechanisms were analyzed and discussed. Moreover, the microstructure, mechanical properties, degradation behaviors and cell responses of the scaffolds were also assessed.

2. Materials and Methods

2.1 Powders Preparation

PHBV with 3 mol% of 3-hydroxyvalerate content, 280 kDa of molecular weight, 1 μm of average particle size and 1.25 g/cm^3 of density (the data were provided by the manufacturer) was obtained from Tianan Biologic Materials Co., Ltd. (Ningbo, China). nMgO with average particle size of 50 nm and density of 3.58 g/cm^3 (the data were provided by the manufacturer) was purchased from Shanghai Macklin Biochemical Co., Ltd. (Ningbo, China).

Five formulations of PHBV/nMgO powders containing 0, 1, 3, 5 and 7 wt% nMgO were prepared mainly through the following procedures[21]: (a) weighing certain amounts of PHBV and nMgO powders according to the designed formulations, and adding them into two beakers containing certain amounts of absolute ethyl alcohol, respectively, followed by magnetically stirring the two solutions for 30 min, respectively; (b) adding the nMgO solution into the PHBV solution, and magnetically stirring the mixed solution for 30 min, followed by ultrasonically dispersing for 30 min; (c) filtering the mixed solution to obtain the mixed powders; (d) drying the mixed powders in vacuum drying oven at 60 °C for 24 h; (e) mechanically milling the dried powders with planetary ball mill for 2 h, and finally obtaining the PHBV/nMgO powders.

2.2 Scaffolds Preparation

Three-dimensional porous scaffolds were prepared *via* a self-developed SLS system, which consisted mainly of a CO_2 laser device (SR 10i, Rofin-Sinar Laser GmbH, Hamburg, Germany) and a galvanometer scanning system (3D scanhead-300-15D, Beijing Century Sunny Technology Co., Beijing, China). Briefly, the laser selectively sinters the powder layers under the control of the scanning system according to the cross-section profiles of the designed parts, forming the solid parts in a layer-by-layer manner[22,23]. The primary processing parameters, *i.e*., laser power, scanning speed, scanning spacing and layer thickness were set as 2 W, 200 mm/s, 0.1 mm and 0.1 mm, respectively. Five formulations of PHBV/nMgO scaffolds containing 0, 1, 3, 5 and 7 wt% nMgO were fabricated, which were denoted as PHBV, PHBV/1%nMgO, PHBV/3%nMgO, PHBV/5%nMgO and PHBV/7%nMgO scaffolds, respectively.

2.3 Microstructures and Mechanical Properties

The phase composition of the PHBV/nMgO scaffolds was analyzed by X-ray diffraction (XRD) (Bruker D8, German Bruker Co., Karlsruhe, Germany). The diffraction data were collected from 5 to 70° at a scan rate of 8°/min using Ni-filtered Cu Kα radiation (λ = 1.5406 Å). The surface morphologies of the PHBV/nMgO scaffolds were analyzed by scanning electron microscope (SEM) (MIRA3, TESCAN, Brno, Czech Republic) installed with energy dispersive spectroscopy (EDS) (X-Max 20, Oxford Instruments, UK) using secondary electron model under 15 kV accelerating voltage. Before the characterization, the specimens were fixed on copper stubs using electrically conductive adhesives, followed by spurting with platinum to increase their conductivity.

The mechanical properties of the PHBV/nMgO scaffolds were assessed by compression tests using a universal testing machine with a 30 kN load cell (MTS Insight 30, MTS Systems Corporation, MN, USA). The specimens (cylinder, 12.7 mm in diameter by 25.4 mm) were compressed to 50% strain at a rate of 1 mm/min[24,25]. The compressive strength and compressive modulus of the scaffolds were determined from the obtained compressive stress-strain curves. Five specimens were tested for each formulation of the scaffolds. The scaffolds with optimal compressive properties were then used to characterize their antibacterial activity, degradation properties and cytocompatibility.

2.4 Antibacterial Activity

E. coli was used as a model bacterium as it is one of the most common bacteria causing orthopedic implant-related infections[26]. The antibacterial activity was evaluated by seeding *E. coli* ATCC 25922 to the PHBV/5%nMgO scaffolds and then observing the

adhesion and proliferation level, with PHBV scaffolds serving as control. The bacterial suspensions were diluted to a concentration of 5×10^5 CFU/mL as this is the clinically relevant concentration in orthopedic infections[27]. Before seeding, the scaffold specimens (diameter 8 mm, thickness 4 mm) were sterilized in XFS-260 autoclave at 120 °C for 20 min, followed by immersing in phosphate buffer solution (PBS) overnight to prewet. Afterwards, the specimens were seeded with the diluted bacterial suspensions and incubated in low glucose Dulbecco's Modified Eagle Medium (DMEM) at 37 °C in 5% CO_2/95% air atmosphere. After 24 h of incubation, the bacterium/scaffold constructs were gently washed using PBS, and then were fixed with 2.5% glutaraldehyde. Subsequently, they were dehydrated with a graded ethanol series, and dried in vacuum drying oven. Afterwards, the dried specimens were installed on copper stubs, sputtering with platinum. Finally, the adhesion and proliferation level of *E. coli* were characterized using a SEM (Phenom ProX, Phenom-World BV, Netherlands) installed with EDS (INCA, Oxford Instruments, UK) under backscattering mode.

Reactive oxygen species (ROS) was reported to play a significant role in exerting the antibacterial activity of some metallic oxide including nMgO[12,13]. Hence, an oxidation-reduction method[28,29] based on reducing nitroblue tetrazolium (NBT) by ROS was employed to detect the production of ROS in the suspensions containing PHBV/5%nMgO scaffolds, with PHBV scaffolds serving as control. Firstly, approximately 50 mg PHBV/5%nMgO scaffold specimens were added into a cap-sealed tube filling with 50 mL PBS containing 2.5×10^{-5} M NBT, followed by incubating at 37 °C in a water bath shaker (SHA-C, Hunan Lichen Instrument Technology Co., Ltd., Changsha, China). After incubating for 1 min, 1 mL of the suspension was aspirated and filtered in order to determine the initial absorbance. After that, another 1 mL of the suspension was regularly aspirated and filtered at a fixed time interval of 10 min until 60 min. The absorbance of the initial filtrates and the filtrates taken out at the fixed time interval was measured with an ultraviolet-visible (UV-vis) spectrophotometer at 259 nm where NBT showed a maximum absorbance. The amount of the produced ROS was proportional to the reduction percentage of NBT, which was calculated by the equation (2.1):

$$\text{Reduction percentage of NBT (\%)} = (A_0-A_t)/A_0\times100 \quad (2.1)$$

where A_0 and A_t represent the absorbance of the initial filtrates and the filtrates taken out at *t* min, respectively. The ROS detection tests were performed in quintuplicate. Besides, a blank control was also set, where no scaffold specimens were added into PBS/NBT solution, in order to exclude the effects of possible self-decomposition of NBT.

2.5 Degradation Properties

The degradation properties of the PHBV/nMgO scaffolds were evaluated by immersing them in PBS (pH = 7.4). Prior to immersion, the initial weights of the specimens were recorded. Approximately 1 g specimen was added into a cap-sealed tube containing 10 mL PBS and incubated in an electronic thermostat water bath at 37 °C. After the predetermined immersion time (7, 14, 21, 28 and 35 days), the specimens were taken out and the PBS was collected. The pH values of the collected PBS were measured using a digital pH meter with a resolution of 0.01 (PHS-3C, Shanghai Xiaosheng Instrument Manufacturing Co., Ltd., Shanghai, China). The specimens were dried in a vacuum drying oven until their weights were constant. The weight loss of the specimens was calculated by the equation (2.2):

$$\text{Weight loss (\%)} = (W_0-W_t)/W_0\times100 \quad (2.2)$$

where W_0 and W_t represents the initial weights and the residual weights of the specimens after t days of immersion, respectively. The pH and weight loss tests were carried out in quintuplicate.

After the weight loss was determined, the specimens were used to characterize the degradation morphologies. Before SEM characterization, the specimens were installed on copper stubs and sputtered with gold. The surface morphologies of the specimens were observed by Phenom ProX SEM using backscattering mode under 15 kV acceleration voltage.

2.6 Cytocompatibility

The cytocompatibility of PHBV/5% nMgO scaffold was evaluated by seeding with MG63 cells (American Type Culture Collection, Manassas, VA, USA) and assessing the cellular responses. The MG63 cells were harvested using trypsin/EDTA, centrifuged at 1×10^3 rpm for 3 min and resuspended in DMEM. The scaffold specimens (diameter 8 mm, thickness 4 mm) were sterilized in an autoclave (XFS-260, Zhejiang Xinfeng Medical Devices Co., Ltd., Shaoxing, China) at 120 °C for 20 min, followed by immersing in PBS overnight to prewet. Afterwards, the specimens were seeded with MG63 cells (at a density of 2×10^3/well, 1×10^5/well and 5×10^5/well for SEM observation, Cell Counting Kit-8 (CCK-8) assay and alkaline phosphatase (ALP) staining, respectively) and incubated in low glucose DMEM supplemented with 10% fetal bovine serum and 1% antibiotic-antimycotic solution at 37 °C in 5% CO_2/95% air atmosphere. After the selected incubation time, the cell-scaffold constructs were sacrificed to assess the cellular adhesion, proliferation and osteogenic

differentiation by SEM observation, CCK-8 assay and ALP staining, respectively.

For evaluating cellular adhesion, the cell/scaffold specimens were gently washed with PBS, followed by fixing with 2.5% glutaraldehyde. Subsequently, a graded ethanol series was used to dehydrate the cells. Afterwards, the specimens were dried in vacuum drying oven, followed by sputtering with platinum. Finally, the cellular morphologies were characterized by Phenom ProX SEM using backscattering mode under 15 kV acceleration voltage. For CCK-8 assay, the MG63 cells were harvested from the scaffold specimens by Trypsin-ethylene diamine tetraacetic acid solution, followed by centrifugation treatment. Afterwards, 0.2 mL of the obtained supernatant was added into 1 mL of fresh culture medium, followed by adding CCK-8 (CK04-13, Dojindo Molecular Technologies, Kimamoto, Japan) solution into it according to the instructions of the manufacturer, which generated an orange formazan product by cellular dehydrogenases. After culture for 4 h at 37 °C, 100 µL of the sample solution was transferred into plate to measure the absorbance with a microplate reader (Beckman, USA) at 450 nm. For ALP staining, the MG63 cells were washed with PBS, fixed with 4% paraformaldehyde for 30 min and then permeated with 0.5% Triton X-100 for 30 min. Subsequently, ALP staining was carried out with 5-bromo-4-chloro-3-indolyl-phosphate/NBT (BCIP/NBT) alkaline phosphatase color development kit (P0321, Shanghai Beyotime Biological Technology Co., Ltd, China) according to the instructions of the manufacturer. Finally, the stained cells were mounted with water-based mounting medium (Boster Biological Technology Co., Ltd., China), followed by observing with light microscope.

2.7 Statistical Analysis

Quantitative data were expressed as the mean ± standard deviation. Levene's test was applied to examine equality of variances. Unpaired two-tailed Student's *t*-test was performed to determine statistical significance. Labels *, ** and *** represent $p < 0.05$, $p < 0.01$ and $p < 0.001$, respectively.

3. Results and Discussion

The three-dimensional porous scaffold model and a representative SLS-fabricated PHBV/nMgO scaffold were shown in Figure 1. It could be seen that the shape and size of the scaffold were consistent with those of the model. The scaffold showed a well ordered and interconnected porous structure. It was considered that the pore size of scaffolds should be large enough to ensure nutrient delivery and tissue ingrowth but not too large to prevent cell migration[30]. Roosa *et al.*[31] found all of the polycaprolactone scaffolds with pore size from 350 to 800 µm could promote bone regeneration and there were no significant differences in new bone formation between them. Similar results were reported by Schek *et al.*[32] who found significant new bone formation for both poly(propylenefumarate)/β-tricalcium phosphate scaffolds with 300 and 800 µm pores, with no statistical differences between them. Hence, the PHBV/nMgO scaffold with pore size of about 400 µm may be beneficial for substance metabolism, cell responses and bone regeneration.

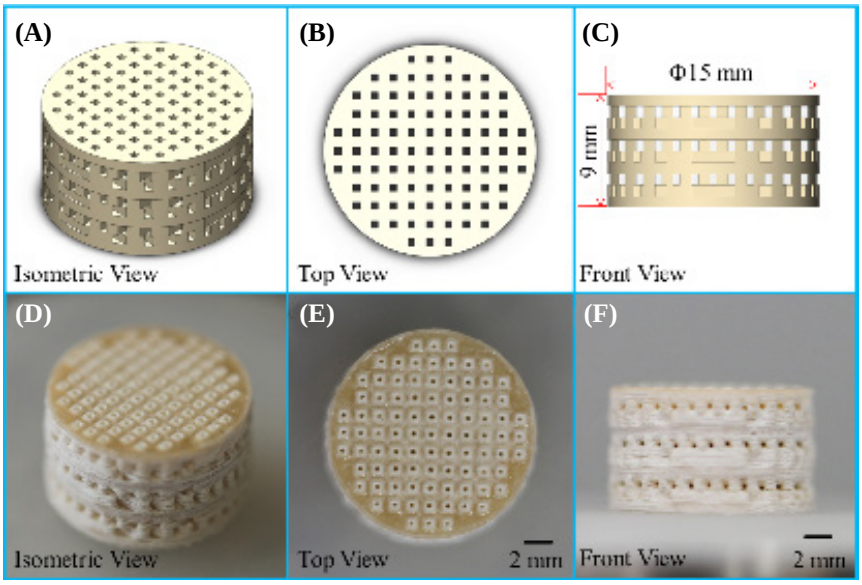

Figure 1. (**A**–**C**) The three-dimensional porous scaffold model and (**D**–**F**) a representative SLS-fabricated PHBV/nMgO scaffold.

The XRD patterns of the PHBV/nMgO scaffolds were plotted in Figure 2. The PHBV scaffold showed strong diffraction peaks at 2θ = 13.4 and 16.8°, which were corresponding to (020) and (110) planes, respectively; additional diffraction peaks at 2θ = 20.1, 21.4, 22.6, 25.5, and 27.1° were also detected, which were assigned to (021), (101), (111), (121), and (040) planes, respectively[33,34]. After incorporating nMgO, the scaffolds showed two new diffraction peaks at 2θ = 42.9 and 62.3°, which were just corresponding to the two main diffraction peaks of MgO assigning to (200) and (220) planes (JCPDS 87-0653), respectively. Moreover, the intensities of the main diffraction peaks of nMgO gradually increased with increasing nMgO content. This indicated nMgO kept thermal stability during the SLS process as it had a very high melting point more than 2800 °C[35].

The compressive strength and compressive modulus of the PHBV/nMgO scaffolds as a function of nMgO content were depicted in Figure 3. In general, they both increased at first but decreased then with the nMgO content increasing from 0 to 7 wt%. The compressive strength and compressive modulus of the PHBV scaffolds were 2.62 and 29.33 MPa, respectively. After incorporating nMgO from 1 to 5 wt%, they keep increasing from 3.37 to 5.14 MPa, and 34.36 to 44.68 MPa, respectively. However, they began to decrease when the nMgO content exceeded 5 wt%. Therefore, the optimal nMgO content was considered to be 5 wt% to obtain the optimal compressive strength and modulus, which were improved by 96.18% and 52.34% compared with the PHBV scaffolds, respectively. It was worth noting that the optimal compressive strength and modulus of the scaffolds was close to that of human trabecular bone (4 to12 MPa and 50 to 500 MPa, respectively[36]).

As the dispersion of fillers in polymer matrix was a significant factor influencing the mechanical properties of polymer composites[37–40], the dispersion of nMgO in PHBV matrix with different nMgO content were characterized using SEM (Figure 4). After incorporation of nMgO, some bright spots appeared in the PHBV matrix; their amounts gradually increased with the nMgO content increasing. The EDS spectrums indicated that the bright spots were just the nMgO incorporated. They kept dispersing uniformly in the PHBV matrix until 5 wt%. However, severe aggregations happened when further increasing the nMgO content. It was well known that excessive nanoparticles would easily result in the occurrence of agglomeration due to the large specific surface area and surface energy[41,42].

The compressive properties of the PHBV/nMgO scaffolds increased with the nMgO content increasing as the total interfacial areas between the fillers and matrix keep increasing. The significant improvements in the mechanical properties of the PHBV/nMgO scaffolds were resulted from strong reinforcing effects of MgO nanoparticles. There were several factors accounting for it: (a) the elastic modulus of MgO was as high as 310 GPa[43], ensuring the applied stress could be transferred to the fillers from the matrix; (b) the nano-sized MgO have extremely high specific surface area, which greatly increased their interfacial areas with the matrix and thus enhanced effectiveness of the stress transfer; (c) the uniform dispersion of MgO nanoparticles in the PHBV matrix maximized its potential in improving the mechanical properties. However, excessive nanoparticles would form severe agglomerations (>5 wt%), which

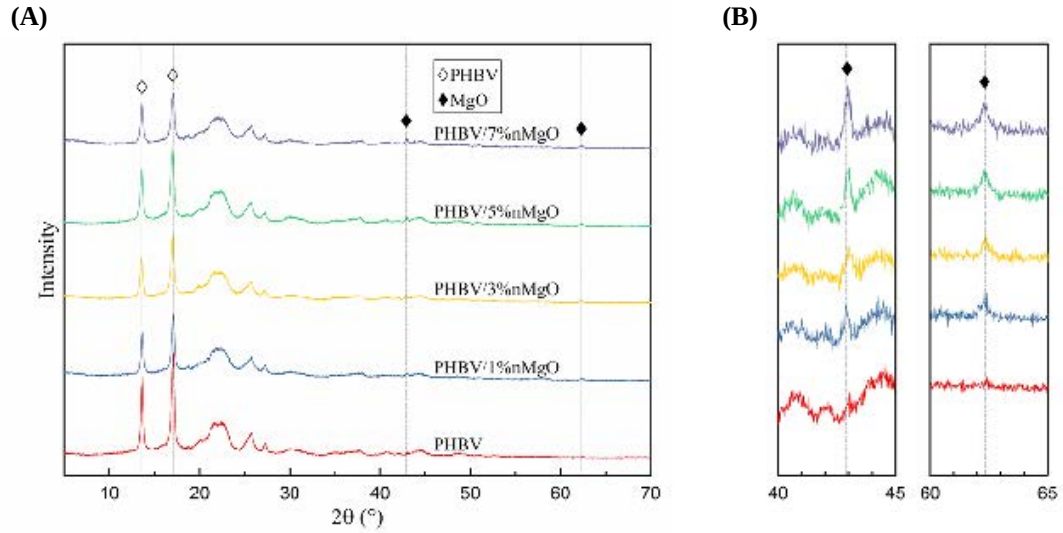

Figure 2. (**A**) The XRD patterns of the PHBV/nMgO scaffolds; (**B**) the enlarged version from 40° to 45° and 60° to

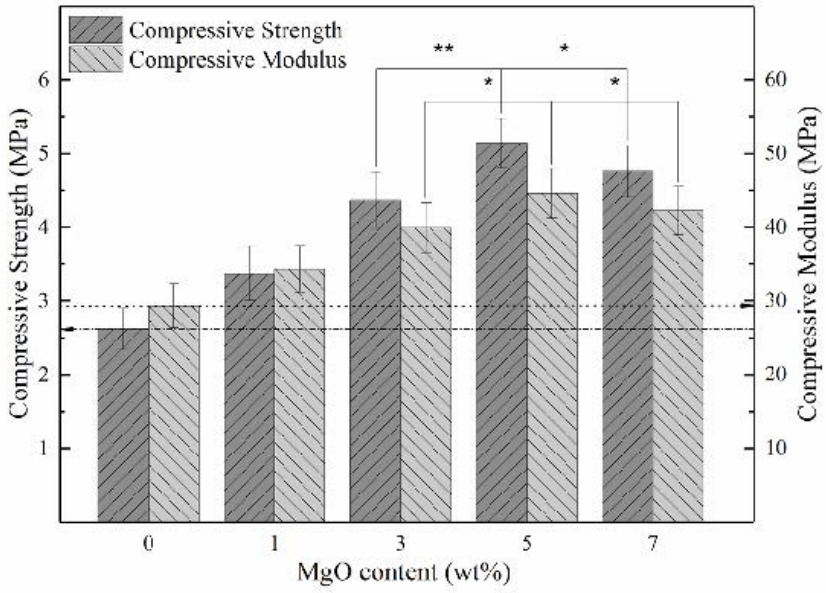

Figure 3. The compressive strength and compressive modulus of the PHBV/nMgO scaffolds as a function of nMgO content

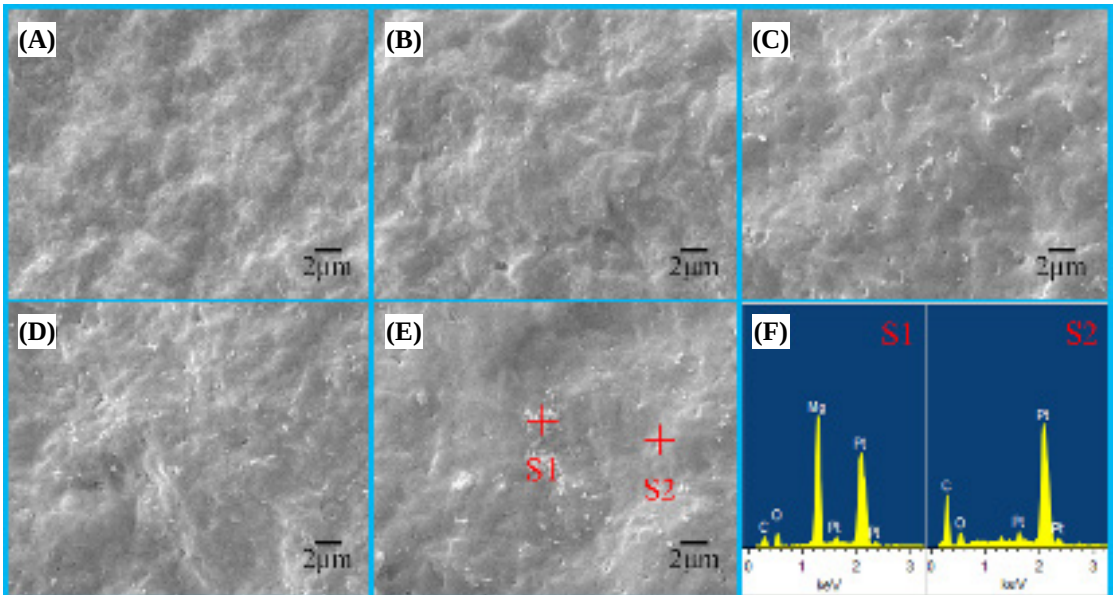

Figure 4. The distribution of nMgO in PHBV matrix with (**A**) 0, (**B**) 1, (**C**) 3, (**D**) 5 and (**E**) 7 wt% nMgO; (**F**) the EDS spectrums of point S1 and S2.

led to a significant decrease of the interfacial areas and strength between the fillers and matrix, thus resulting in the decrease of the reinforcing efficiency. As the PHBV/5%nMgO scaffold showed optimal compressive properties, they were selected to be further evaluated in terms of antibacterial activity, degradation behaviors and cytocompatibility.

The adhesion and proliferation level of *Escherichia coli* (*E. coli*) cultured on the PHBV/5%nMgO and PHBV scaffolds after 24 h were evaluated by SEM (Figure 5). The *E. coli* showed a typical rod shape. It was obvious that large amounts of *E. coli* attached on the PHBV scaffolds and covered almost the entire surface. In contrast, there was only a small amount of *E. coli* attaching on the PHBV/5%nMgO scaffolds. The dramatic decrease of the numbers of *E. coli* indicated that nMgO inhibited the adhesion and proliferation of *E. coli* and killed them. Moreover, it seemed the appearance of the *E. coli* attached on the PHBV/nMgO scaffolds was abnormal, suggesting them suffered structural damage from the antibacterial action of nMgO (Figure 5D). The results indicated the incorporation of nMgO imparted strong antibacterial activity to the scaffolds.

As ROS production was reported to play a significant

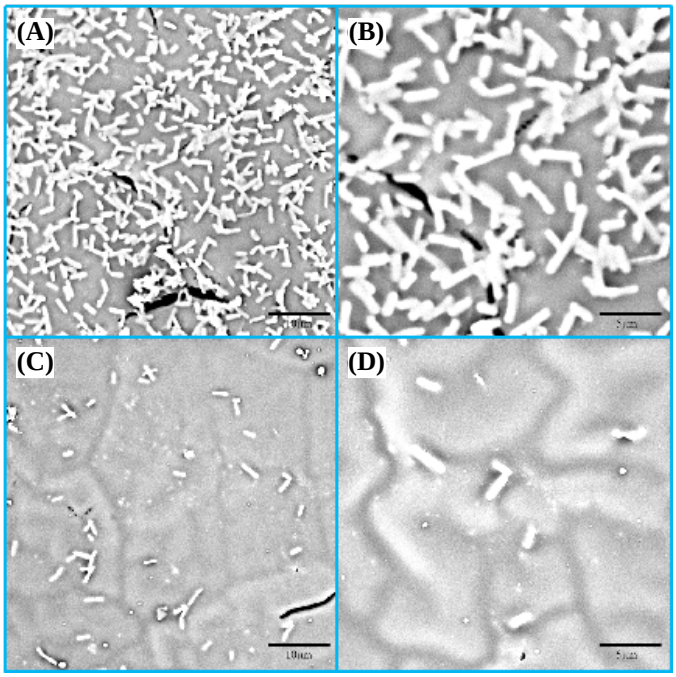

Figure 5. The morphologies of *Escherichia coli* cultured on (**A**, **B**) PHBV and (**C**, **D**) PHBV/5%nMgO scaffolds after 24 h.

role in exerting the antibacterial activity of some metallic oxide including nMgO[44–46]. Hence, the production of ROS from the PHBV/nMgO scaffolds was indirectly determined by calculating the reduction percentage of NBT. As shown in Figure 6, there was almost no reduction of NBT for PHBV scaffolds, indicating they did not produce ROS. Actually, a slight reduction of ROS could be observed, which was resulted from the decomposition of NBT itself as shown in the blank control. In contrast, there happened significant reduction of NBT for the PHBV/nMgO scaffolds. Meanwhile, the reduction of NBT gradually increased with incubation time increasing. The results demonstrated nMgO promoted the production of ROS.

The production of ROS may be attributed to a sequential oxidation-reduction reactions occurred at the surface of nMgO[47]. In detail, nMgO could be hydrated with water and form $Mg(OH)_2$ on its surface, leading to the formation of surface bound electron-hole pairs, which would subsequently decompose into surface trapped electrons and localized holes[48,49]. They were typical oxide catalysts and would promote molecular oxygen (O_2) to produce ROS *via* single electron reduction[50]. It was worth noting that ROS was a strong oxidant. When its concentration exceeded the scavenging ability of the antioxidant defense system of bacteria,

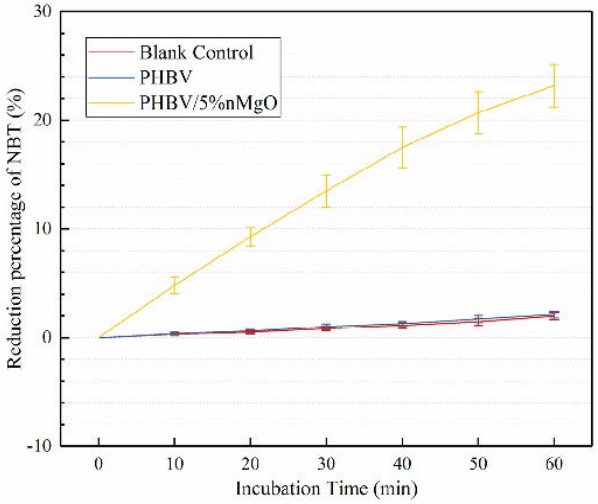

Figure 6. Reduction percentage of NBT with different incubation time for PHBV/5%nMgO and PHBV

they would compel them generate oxidative stress, which subsequently led to the damage of the structure and functions of bacteria[51,52]. Besides, the contact action of the MgO nanoparticles on bacteria would make them generate mechanical stress, resulting in the deformation and damage of the bacterial structure[53,54]. In addition, there were large amounts of active sites on MgO nanoparticles[55], enabling them easily absorb to the bacteria; the enrichment of nanoparticles on the bacteria would increase their membrane permeability[56]. The possible antibacterial mechanisms of nMgO were summarized in detail in Figure 7.

The mass loss and pH for the PHBV/5%nMgO and PHBV scaffolds after immersion in PBS for different days were shown in Figure 8A and 8B, respectively. The mass loss of both of the scaffolds gradually increased with immersion time prolonging, but it was obvious that the mass loss of the PHBV/5%nMgO scaffolds was larger than that of the PHBV scaffolds. After 35 days, the mass loss of the PHBV/5%nMgO scaffolds was 12.68%, which was almost double that of the PHBV scaffolds. In contrast, the change trends of pH for the PHBV and PHBV/5%nMgO scaffolds were significantly different; the pH for the former decreased gradually while that of the latter increased gradually with immersion time increasing. After 35 days, the pH for the PHBV and PHBV/5%nMgO scaffolds were 6.85 and 7.63, respectively, resulting in a weakly acid and weakly alkaline microenvironment, respectively. Besides, the amplitude of pH variation for the PHBV/5%nMgO scaffolds was much smaller than that for the PHBV scaffolds. This was mainly ascribed to the alkaline degradation products of MgO, which exerted neutralization effect against the acid degradation products of PHBV. These results indicated nMgO could promote the degradation of the PHBV scaffolds and neutralize their acid degradation products.

The surface microtopography of PHBV/5%nMgO and PHBV scaffolds after immersion were characterized by SEM (Figure 9) to explain the results of mass loss and pH. It was clear that the surface morphologies of the PHBV/5%nMgO scaffolds were significantly different from that of PHBV scaffolds. In general, the surfaces of PHBV scaffolds after immersion were smooth if the microvoids and microcracks on them were neglected. For PHBV/5%nMgO scaffolds, many micropores appeared on the surface after 7 days of immersion. With the degradation time prolonging, their quantity and size gradually increased. After 35 days of degradation, large amounts of pores formed on the surface, resulting in a microporous structure.

The micropores were resulted from the degradation of MgO nanoparticles as well as the subsequent collapse of the PHBV matrix. It was known that MgO would be hydrolyzed with water to form $Mg(OH)_2$, but a strange thing was that it seemed no $Mg(OH)_2$ particles appeared on the surface. Nevertheless, the EDS mapping results (Figure 9G) indicated that there obviously existed element Mg after degradation, which belonged to $Mg(OH)_2$ and/or MgO in the PHBV matrix. The "disappearance" of $Mg(OH)_2$ was attributed to its dissolution and outflow into PBS solutions. When

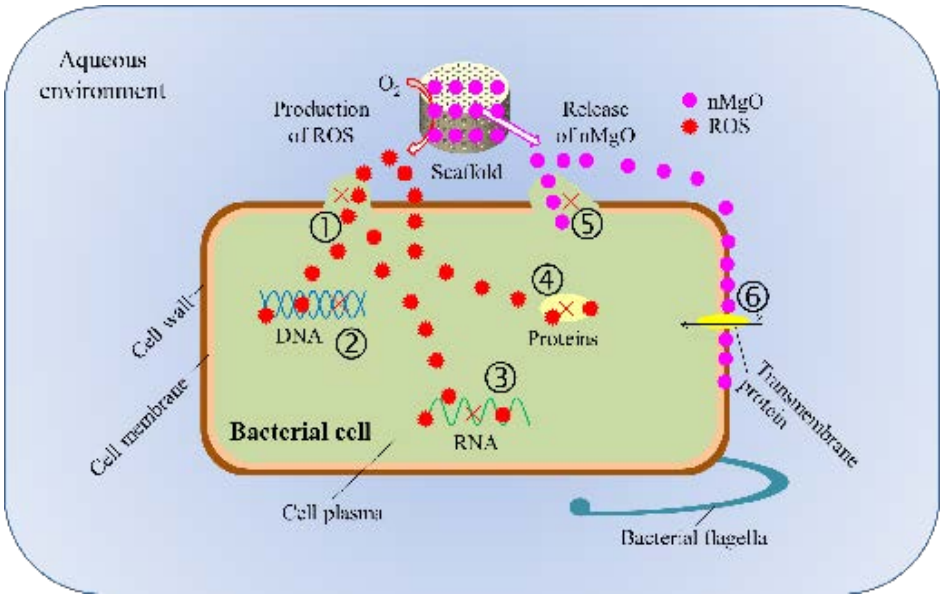

Figure 7. Possible antibacterial mechanisms of the PHBV/nMgO scaffolds: (1) oxidative damage of cell wall and membrane of bacteria resulted by ROS; (2) oxidative damage of DNA and inhibition of its transcription resulted by ROS; (3) oxidative damage of RNA and inhibition of its translation resulted by ROS; (4) oxidative damage and activity inhibition of proteins resulted by ROS; (5) mechanical damage of cell wall and/or membrane of bacteria resulted by the contact action of nMgO; (6) change of membrane permeability of bacteria resulted by the enrichment of nMgO.

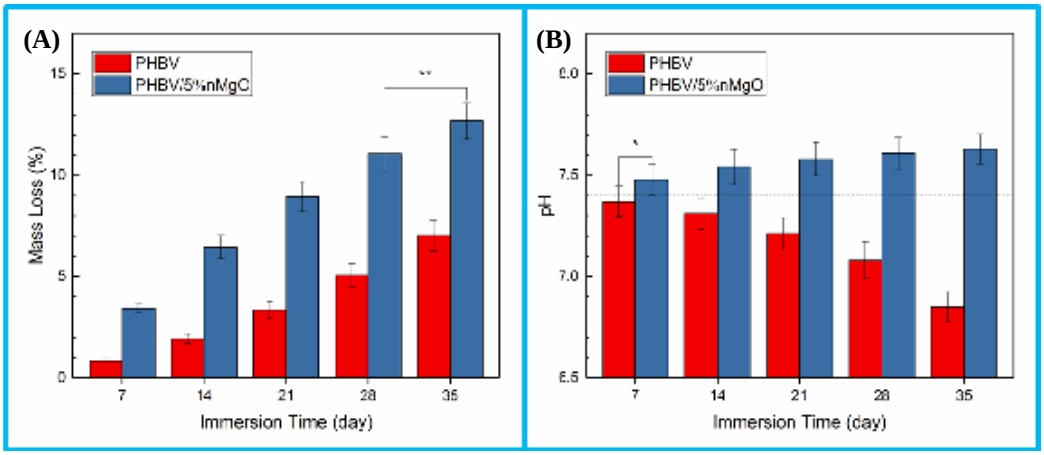

Figure 8. The (**A**) mass loss and (**B**) pH for the PHBV/5%nMgO and PHBV scaffolds as a function of immersion

MgO was hydrated with water to form $Mg(OH)_2$, its crystal lattice would transform from cubic structure to hexagonal structure, which resulted in significant volume expansion[57]. Meanwhile, crystal growth pressure and water-absorbing swelling pressure of $Mg(OH)_2$ would further promote the volume expansion[58]. This would lead to the deterioration of the interface adhesion between the particles and matrix, thus making them easy to outflow and leave large amounts of micropores in the matrix. In return, the pores would significantly increase the specific surface area of the matrix and make water permeate more easily, thus promoting the degradation of the scaffolds.

The cytocompatibility of PHBV/5%nMgO scaffolds was evaluated in terms of cellular adhesion, proliferation and osteogenic differentiation. The adhesion morphology of MG63 cells on PHBV/5%nMgO and PHBV scaffolds after culture for 1, 3 and 5 days was shown in Figure 10. MG63 cells showed an elongated shape and anchored to the surface of the PHBV scaffolds with lamellipodia after 1 day of culture. Some of them gathered together and formed clusters on day 3. On day 5, most regions of the PHBV scaffolds were covered with cell clusters. As for PHBV/5%nMgO scaffolds, some of MG63 cells fused together on the surfaces as soon as on day 1. After 5 days of culture, the entire regions of the PHBV/5%nMgO scaffolds were almost fully covered with MG63 cells, forming thicker cell clusters than that

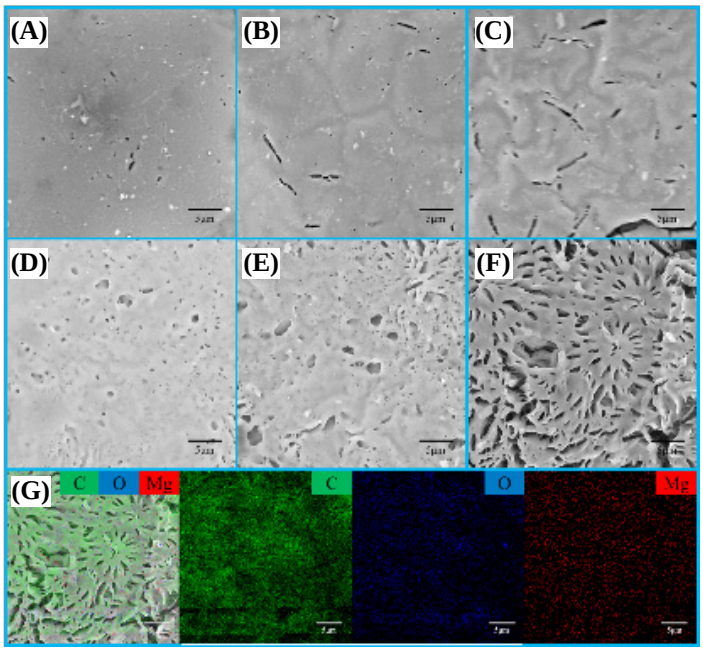

Figure 9. The surface microtopography of (**A**, **B**, **C**) PHBV scaffolds and (**D**, **E**, **F**) PHBV/5%nMgO scaffolds after immersion in PBS for (**A**, **D**) 7, (**B**, **E**) 21 and (**C**, **F**) 35 days; (**G**) the EDS mapping images of carbon, oxygen and magnesium elements for the PHBV/5%nMgO scaffolds after 35 days of immersion.

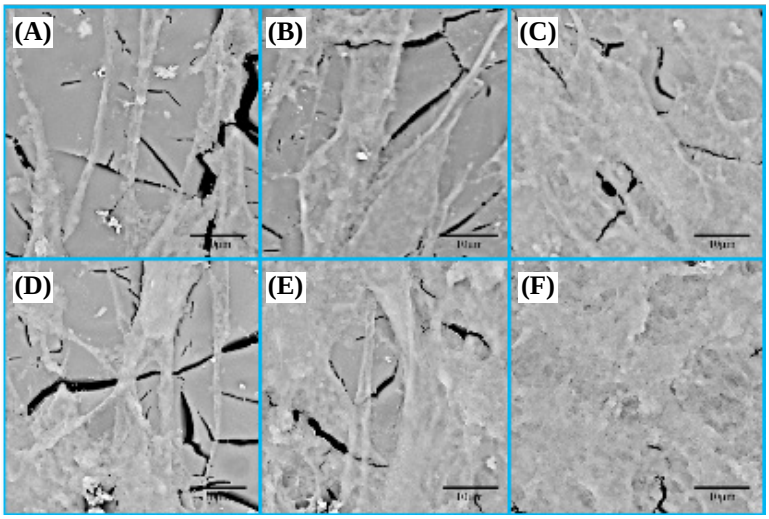

Figure 10. The adhesion morphology of MG63 cells on (**A**, **B**, **C**) PHBV and (**D**, **E**, **F**) PHBV/5%nMgO scaffolds after culture for (**A**, **D**) 1, (**B**, **E**) 3 and (**C**, **F**) 5 days.

on the PHBV scaffolds. The SEM results indicated the addition of MgO promoted the cellular adhesion and proliferation of MG63 cells on the scaffolds.

The proliferation level of MG63 cells on PHBV/5% nMgO and PHBV scaffolds after culture for 1, 3 and 5 days was evaluated by CCK-8 assay (Figure 11). The absorbance is directly proportional to the number of cells according to the principle[59]. It was clear that the number of MG63 cells gradually increased during the whole culture period, for both of the scaffolds. There were significant differences in cell numbers between the adjacent culture time for the PHBV/5% nMgO scaffolds. More importantly, the cell numbers on the PHBV/5% nMgO scaffolds were more than that on the PHBV scaffolds, with significant differences being observed. The CCK-8 assay results suggested the addition of nMgO promoted the proliferation of MG63 cells on the scaffolds.

The osteogenic differentiation of MG63 cells on the PHBV/5% nMgO and PHBV scaffolds was evaluated by ALP staining assay as ALP was widely recognized as a marker for osteogenic differentiation[60]. The number of cells staining positive gradually increased with culture time increasing for both of the PHBV/5% nMgO and PHBV scaffolds (Figure 12). This was attributed either to the maturation of seeded cells or to that of the newly proliferated cells. Furthermore, the cells staining positive on the PHBV/5% nMgO scaffolds were much more than that on the PHBV scaffolds. The ALP staining results indicated the addition of nMgO improved the ability of the scaffolds to induce osteogenic differentiation of MG63 cells.

Ion release from biomaterials was one of the main factors influencing cellular responses[61,62]. It was known that many metal ions could act as co-enzyme factors, thus influencing signal pathways and stimulating cellular responses[63]. In particular, Mg^{2+} could initiate activation of integrins through attaching to the sites on their α-chain[64,65]. It is noted that integrins play an important role in modulating cellular functions such as cellular adhesion, migration, proliferation, differentiation of all human cells as the transduce signals could regulate expression of related genes[66,67]. In the presence of water in the culture medium, the MgO nanoparticles in the matrix would be hydrated with water to form $Mg(OH)_2$. The product would further hydrolyze and ionize into Mg^{2+} and OH^-. Hence, the Mg^{2+} could be released from the scaffolds and be finally utilized by MG63 cells, stimulating their cellular responses.

4. Conclusions

PHBV/nMgO scaffolds fabricated *via* SLS showed interconnected and well-ordered microporous structures. The incorporation of nMgO imparted strong antibacterial activity to the PHBV scaffolds. The antibacterial mechanism was that nMgO could promote the production of ROS and mechanically contact with bacteria. Besides, the compressive strength and compressive modulus of the PHBV scaffolds were increased by 96.18% and 52.34% with addition of 5 wt% nMgO, respectively. Moreover, nMgO could neutralize the acid degradation products of PHBV and promote the degradation of the scaffolds. In addition, nMgO stimulated the cellular adhesion, proliferation and osteogenic differentiation. This study may provide preliminary guidance for applying nMgO as an attractive antibacterial material for bone tissue engineering.

Conflict of Interest and Funding

No conflict of interest was reported by the authors. The

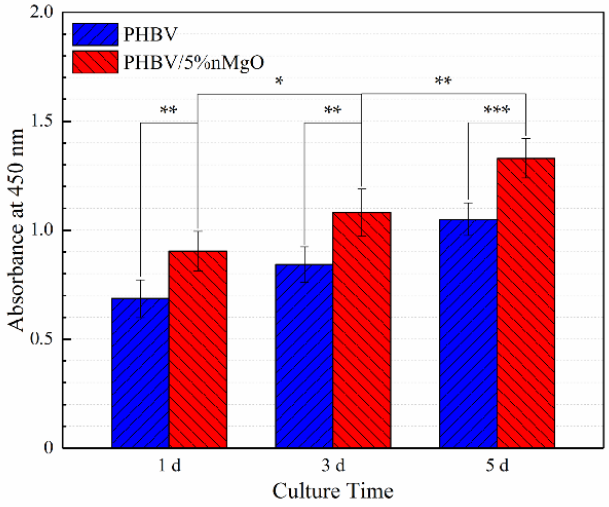

Figure 11. The absorbance for the MG63 cells on the PHBV/5%nMgO and PHBV scaffolds after culture for 1, 3 and 5 days.

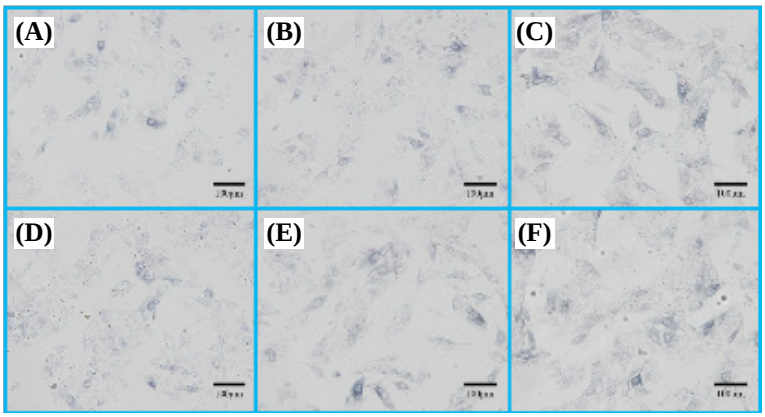

Figure 12. The ALP staining images for (**A**, **B**, **C**) PHBV and (**D**, **E**, **F**) PHBV/5%nMgO scaffolds after culture for (**A**, **D**) 1, (**B**, **E**) 3 and (**C**, **F**) 5 days.

authors gratefully acknowledge the following projects and funds for the financial support: (1) The Natural Science Foundation of China (51575537, 81572577, 51705540); (2) Overseas, Hong Kong, and Macao Scholars Collaborated Researching Fund of National Natural Science Foundation of China (81428018); (3) Hunan Provincial Natural Science Foundation of China (2016JJ1027); (4) The Project of Innovation-driven Plan of Central South University (2016CX023); (5) The Open-End Fund for the Valuable and Precision Instruments of Central South University; (6) The fund of the State Key Laboratory of Solidification Processing at NWPU (SKLSP201605); (7) The Project of State Key Laboratory of High Performance Complex Manufacturing, Central South University, and (8) National Postdoctoral Program for Innovative Talents (BX201700291).

References

1. Zimmerli W, 2014, Clinical presentation and treatment of orthopaedic implant-associated infection. *J Intern Med*, 276(2): 111–119. http://dx.doi.org/10.1111/joim.12233
2. Saidin S, Chevallier P, Abdul Kadir M R, *et al.*, 2013, Polydopamine as an intermediate layer for silver and hydroxyapatite immobilisation on metallic biomaterials surface. *Mater Sci Eng C Mater Biol Appl*, 33(8): 4715–4724. http://dx.doi.org/10.1016/j.msec.2013.07.026
3. Lorenzetti M, Dogsa I, Stosicki T, *et al.*, 2015, The influence of surface modification on bacterial adhesion to titanium-based substrates. *ACS Appl Mater Interfaces*, 7(3): 1644–1651. http://dx.doi.org/10.1021/am507148n
4. Overbye K, Barrett J, 2005, Antibiotics: Where did we go wrong? *Drug Discov Today*, 10(1): 45–52. http://dx.doi.org/10.1016/s1359-6446(04)03285-4

5. Londonkar R L, Madire Kattegouga U, Shivsharanappa K, *et al.*, 2013, Phytochemical screening and *in vitro* antimicrobial activity of *Typha angustifolia* Linn leaves extract against pathogenic gram negative micro organisms. *J Pharm Res*, 6(2): 280–283. http://dx.doi.org/10.1016/j.jopr.2013.02.010
6. Trampuz A, Zimmerli W, 2006, Antimicrobial agents in orthopaedic surgery. *Drugs*, 66(8): 1089–1106. http://dx.doi.org/10.2165/00003495-200666080-00005
7. Goodman S B, Yao Z, Keeney M, *et al.*, 2013, The future of biologic coatings for orthopaedic implants. *Biomaterials*, 34(13): 3174–3183. http://dx.doi.org/10.1016/j.biomaterials.2013.01.074
8. Yang S, Zhang Y, Yu J, *et al.*, 2014, Antibacterial and mechanical properties of honeycomb ceramic materials incorporated with silver and zinc. *Mater Des*, 59: 461–465. http://dx.doi.org/10.1016/j.matdes.2014.03.025
9. Yazdimamaghani M, Vashaee D, Assefa S, *et al.*, 2014, Hybrid macroporous gelatin/bioactive-glass/nanosilver scaffolds with controlled degradation behavior and antimicrobial activity for bone tissue engineering. *J Biomed Nanotechnol*, 10(6): 911–931. http://dx.doi.org/10.1166/jbn.2014.1783
10. Sánchez-Salcedo S, Shruti S, Salinas A J, *et al.*, 2014, *In vitro* antibacterial capacity and cytocompatibility of SiO_2–CaO–P_2O_5 meso-macroporous glass scaffolds enriched with ZnO. *J Mater Chem B*, 2(30): 4836–4847. http://dx.doi.org/10.1039/c4tb00403e
11. Vargas-Reus M A, Memarzadeh K, Huang J, *et al.*, 2012, Antimicrobial activity of nanoparticulate metal oxides against peri-implantitis pathogens. *Int J Antimicrob Agents*, 40(2): 135–139. http://dx.doi.org/10.1016/j.ijantimicag.2012.04.012
12. Dizaj S M, Lotfipour F, Barzegar-Jalali M, *et al.*, 2014, Antimicrobial activity of the metals and metal oxide nanoparticles. *Mater Sci Eng C Mater Biol Appl*, 44: 278–284. http://dx.doi.org/10.1016/j.msec.2014.08.031
13. Li Y, Zhang W, Niu J, *et al.*, 2012, Mechanism of photogenerated reactive oxygen species and correlation with the antibacterial properties of engineered metal-oxide nanoparticles. *ACS Nano*, 6(6): 5164–5173. http://dx.doi.org/10.1021/nn300934k
14. Krishnamoorthy K, Moon J Y, Hyun H B, *et al.*, 2012, Mechanistic investigation on the toxicity of MgO nanoparticles toward cancer cells. *J Mater Chem*, 22(47): 24610–24617. http://dx.doi.org/10.1039/c2jm35087d
15. Staiger M P, Pietak A M, Huadmai J, *et al.*, 2006, Magnesium and its alloys as orthopedic biomaterials: A review. *Biomaterials*, 27(9): 1728–1734. http://dx.doi.org/10.1016/j.biomaterials.2005.10.003
16. De Silva R T, Mantilaka M M, Ratnayake S P, *et al.*, 2017, Nano-MgO reinforced chitosan nanocomposites for high performance packaging applications with improved mechanical, thermal and barrier properties. *Carbohydr Polym*, 157: 739–747. http://dx.doi.org/10.1016/j.carbpol.2016.10.038
17. Zhao Y, Liu B, You C, *et al.*, 2016, Effects of MgO whiskers on mechanical properties and crystallization behavior of PLLA/MgO composites. *Mater Des*, 89: 573–581. http://dx.doi.org/10.1016/j.matdes.2015.09.157
18. Haldorai Y, Shim J-J, 2014, An efficient removal of methyl orange dye from aqueous solution by adsorption onto chitosan/MgO composite: A novel reusable adsorbent. *Appl Surf Sci*, 292: 447–453. http://dx.doi.org/10.1016/j.apsusc.2013.11.158
19. Yamamoto O, Ohira T, Alvarez K, *et al.*, 2010, Antibacterial characteristics of $CaCO_3$–MgO composites. *Mater Sci Eng B*, 173(1–3): 208–212. http://dx.doi.org/10.1016/j.mseb.2009.12.007
20. Ma F, Lu X, Wang Z, *et al.*, 2011, Nanocomposites of poly(L-lactide) and surface modified magnesia nanoparticles: Fabrication, mechanical property and biodegradability. *J Phys Chem Solids*, 72(2): 111–116. http://dx.doi.org/10.1016/j.jpcs.2010.11.008
21. Feng P, Peng S, Wu P, *et al.*, 2016, A space network structure constructed by tetraneedlelike ZnO whiskers supporting boron nitride nanosheets to enhance comprehensive properties of poly (L-lacti acid) scaffolds. *Sci Rep*, 6: 33385. http://dx.doi.org/10.1038/srep33385
22. Lee J M, Sing S L, Tan E Y S, *et al.*, 2016, Bioprinting in cardiovascular tissue engineering: A review. *Int J Bioprint*, 2(2): 27–36. http://dx.doi.org/10.18063/IJB.2016.02.006
23. Murphy C, Kolan K, Li W, *et al.*, 2017, 3D bioprinting of stem cells and polymer/bioactive glass composite scaffolds for bone tissue engineering. *Int J Bioprint*, 3(1): 54–64. http://dx.doi.org/10.18063/IJB.2017.01.005
24. Eshraghi S, Das S, 2010, Mechanical and microstructural properties of polycaprolactone scaffolds with 1-D, 2-D, and 3-D orthogonally oriented porous architectures produced by selective laser sintering. *Acta Biomater*, 6(7): 2467–2476. http://dx.doi.org/10.1016/j.actbio.2010.02.002
25. Eshraghi S, Das S, 2012, Micromechanical finite-element modeling and experimental characterization of the compressive mechanical properties of polycaprolactone–hydroxyapatite composite scaffolds prepared by selective laser sintering for bone tissue engineering. *Acta Biomater*, 8(8): 3138–3143. http://dx.doi.org/10.1016/j.actbio.2012.04.022

26. Amalric J, Mutin P H, Guerrero G, *et al*., 2009, Phosphonate monolayers functionalized by silver thiolate species as antibacterial nanocoatings on titanium and stainless steel. *J Mater Chem*, 19(1): 141–149. http://dx.doi.org/10.1039/b813344a
27. Simchi A, Tamjid E, Pishbin F, *et al*., 2011, Recent progress in inorganic and composite coatings with bactericidal capability for orthopaedic applications. *Nanomedicine*, 7(1): 22–39. http://dx.doi.org/10.1016/j.nano.2010.10.005
28. Ye L, Liu J, Jiang Z, *et al*., 2013, Facets coupling of BiOBr-g-C_3N_4 composite photocatalyst for enhanced visible-light-driven photocatalytic activity. *Appl Catal B*, 142–143: 1–7. http://dx.doi.org/10.1016/j.apcatb.2013.04.058
29. Wu D, Wang B, Wang W, *et al*., 2015, Visible-light-driven BiOBr nanosheets for highly facet-dependent photocatalytic inactivation of *Escherichia coli*. *J Mater Chem A*, 3(29): 15148–15155. http://dx.doi.org/10.1039/c5ta02757h
30. Bruzauskaite I, Bironaite D, Bagdonas E, *et al*., 2016, Scaffolds and cells for tissue regeneration: Different scaffold pore sizes-different cell effects. *Cytotechnology*, 68(3): 355–369. http://dx.doi.org/10.1007/s10616-015-9895-4
31. Roosa S M, Kemppainen J M, Moffitt E N, *et al*., 2010, The pore size of polycaprolactone scaffolds has limited influence on bone regeneration in an *in vivo* model. *J Biomed Mater Res A*, 92(1): 359–368. http://dx.doi.org/10.1002/jbm.a.32381
32. Schek R M, Wilke E N, Hollister S J, *et al*., 2006, Combined use of designed scaffolds and adenoviral gene therapy for skeletal tissue engineering. *Biomaterials*, 27(7): 1160–1166. http://dx.doi.org/10.1016/j.biomaterials.2005.07.029
33. Ten E, Jiang L, Wolcott M P, 2012, Crystallization kinetics of poly(3-hydroxybutyrate-co-3-hydroxyvalerate)/cellulose nanowhiskers composites. *Carbohydr Polym*, 90(1): 541. http://dx.doi.org/10.1016/j.carbpol.2012.05.076
34. Shuai C, Guo W, Gao C, *et al*., 2017, Calcium silicate improved bioactivity and mechanical properties of poly(3-hydroxybutyrate-co-3-hydroxyvalerate) scaffolds. *Polymers*, 9(5): 175. http://dx.doi.org/10.3390/polym9050175
35. Yin Y, Zhang G, Xia Y, 2002, Synthesis and characterization of MgO nanowires through a vapor-phase precursor method. *Adv Funct Mater*, 12(4): 293–298. http://dx.doi.org/10.1002/1616-3028(20020418)12:4<293::aid-adfm293>3.0.co;2-u
36. Hutmacher D W, Schantz J T, Lam C X, *et al*., 2007, State of the art and future directions of scaffold-based bone engineering from a biomaterials perspective. *J Tissue Eng Regen Med*, 1(4): 245–260. http://dx.doi.org/10.1002/term.24
37. Ning N-y, Yin Q-j, Luo F, *et al*., 2007, Crystallization behavior and mechanical properties of polypropylene/halloysite composites. *Polymer*, 48(25): 7374–7384. http://dx.doi.org/10.1016/j.polymer.2007.10.005
38. Li H Y, Tan Y Q, Zhang L, *et al*., 2012, Bio-filler from waste shellfish shell: Preparation, characterization, and its effect on the mechanical properties on polypropylene composites. *J Hazard Mater*, 217–218: 256–262. http://dx.doi.org/10.1016/j.jhazmat.2012.03.028
39. He F, Fan J, Lau S, 2008, Thermal, mechanical, and dielectric properties of graphite reinforced poly(vinylidene fluoride) composites. *Polym Test*, 27(8): 964–970. http://dx.doi.org/10.1016/j.polymertesting.2008.08.010
40. Maity J, Jacob C, Das C K, *et al*., 2008, Direct fluorination of Twaron fiber and the mechanical, thermal and crystallization behaviour of short Twaron fiber reinforced polypropylene composites. *Compos Part A Appl Sci Manuf*, 39(5): 825–833. http://dx.doi.org/10.1016/j.compositesa.2008.01.009
41. Peng D, Qin W, Wu X, *et al*., 2015, Improvement of the resistance performance of carbon/cyanate ester composites during vacuum electron radiation by reduced graphene oxide modified TiO_2. *RSC Adv*, 5(94): 77138–77146. http://dx.doi.org/10.1039/c5ra11113g
42. Liu G, Zhou T, Liu W, *et al*., 2014, Enhanced desulfurization performance of PDMS membranes by incorporating silver decorated dopamine nanoparticles. *J Mater Chem A*, 2(32): 12907. http://dx.doi.org/10.1039/c4ta01778a
43. Lee S-W, Han S M and Nix W D, 2009, Uniaxial compression of fcc Au nanopillars on an MgO substrate: The effects of prestraining and annealing. *Acta Mater*, 57(15): 4404–4415. http://dx.doi.org/10.1016/j.actamat.2009.06.002
44. Applerot G, Lellouche J, Lipovsky A, *et al*., 2012, Understanding the antibacterial mechanism of CuO nanoparticles: Revealing the route of induced oxidative stress. *Small*, 8(21): 3326–3337. http://dx.doi.org/10.1002/smll.201200772
45. Applerot G, Lipovsky A, Dror R, *et al*., 2009, Enhanced antibacterial activity of nanocrystalline ZnO due to increased ROS-mediated cell injury. *Adv Funct Mater*, 19(6): 842–852. http://dx.doi.org/10.1002/adfm.200801081
46. Sawai J, Kojima H, Igarashi H, *et al*., 2000, Antibacterial characteristics of magnesium oxide powder. *World J Microbiol Biotechnol*, 16(2): 187–194. http://dx.doi.org/10.1023/A:1008916209784
47. Krishnamoorthy K, Manivannan G, Kim S J, *et al*., 2012, Antibacterial activity of MgO nanoparticles based on lipid peroxidation by oxygen vacancy. *J Nanopart Res*, 14(9): 1063. http://dx.doi.org/10.1007/s11051-012-1063-6

48. Sterrer M, Diwald O, Knözinger E, 2000, Vacancies and electron deficient surface anions on the surface of MgO nanoparticles. *J Phys Chem B*, 104(15): 3601–3607. http://dx.doi.org/10.1021/jp993924l

49. Berger T, Sterrer M, Stankic S, *et al*., 2005, Trapping of photogenerated charges in oxide nanoparticles. *Mater Sci Eng C*, 25(5–8): 664–668. http://dx.doi.org/10.1016/j.msec.2005.06.013

50. Sterrer M, Berger T, Diwald O, *et al*., 2003, Energy transfer on the MgO surface, monitored by UV-induced H_2 chemisorption. *J Am Chem Soc*, 125(1): 195–199. http://dx.doi.org/10.1021/ja028059o

51. Long T C, Saleh N, Tilton R D, *et al*., 2006, Titanium dioxide (P25) produces reactive oxygen species in immortalized brain microglia (BV2): Implications for nanoparticle neurotoxicity. *Environ Sci Technol*, 40(14): 4346–4352. http://dx.doi.org/10.1021/es060589n

52. Xia T, Kovochich M, Brant J, *et al*., 2006, Comparison of the abilities of ambient and manufactured nanoparticles to induce cellular toxicity according to an oxidative stress paradigm. *Nano Lett*, 6(8): 1794–1807. http://dx.doi.org/10.1021/nl061025k

53. Jin T, He Y, 2011, Antibacterial activities of magnesium oxide (MgO) nanoparticles against foodborne pathogens. *J Nanopart Res*, 13(12): 6877–6885. http://dx.doi.org/10.1007/s11051-011-0595-5

54. Yamamoto O, Sawai J, Kojima H, *et al*., 2002, Effect of mixing ratio on bactericidal action of MgO–CaO powders. *J Mater Sci Mater Med*, 13(8): 789–792. http://dx.doi.org/10.1023/A:1016179225955

55. Jeevanandam P, Klabunde K, 2002, A study on adsorption of surfactant molecules on magnesium oxide nanocrystals prepared by an aerogel route. *Langmuir*, 18(13): 5309–5313. http://dx.doi.org/10.1021/la0200921

56. He Y, Ingudam S, Reed S, *et al*., 2016, Study on the mechanism of antibacterial action of magnesium oxide nanoparticles against foodborne pathogens. *J Nanobiotechnol*, 14(1): 54. http://dx.doi.org/10.1186/s12951-016-0202-0

57. Salomao R, Bittencourt L, Pandolfelli V, 2007, A novel approach for magnesia hydration assessment in refractory castables. *Ceram Int*, 33(5): 803–810. http://dx.doi.org/10.1016/j.ceramint.2006.01.004

58. Mo L, Deng M, Tang M, *et al*., 2014, MgO expansive cement and concrete in China: Past, present and future. *Cem Concr Res*, 57: 1–12. http://dx.doi.org/10.1016/j.cemconres.2013.12.007

59. Shan D, Shi Y, Duan S, *et al*., 2013, Electrospun magnetic poly (L-lactide) (PLLA) nanofibers by incorporating PLLA-stabilized Fe_3O_4 nanoparticles. *Mater Sci Eng C*, 33(6): 3498–3505. http://dx.doi.org/10.1016/j.msec.2013.04.040

60. Marom R, Shur I, Solomon R, *et al*., 2005, Characterization of adhesion and differentiation markers of osteogenic marrow stromal cells. *J Cell Physiol*, 202(1): 41–48. http://dx.doi.org/10.1002/jcp.20109

61. Wang F, Zhai D, Wu C, *et al*., 2016, Multifunctional mesoporous bioactive glass/upconversion nanoparticle nanocomposites with strong red emission to monitor drug delivery and stimulate osteogenic differentiation of stem cells. *Nano Res*, 9(4): 1193–1208. http://dx.doi.org/10.1007/s12274-016-1015-z

62. Zhang J, Zhu Y, 2014, Synthesis and characterization of CeO_2-incorporated mesoporous calcium-silicate materials. *Microporous Mesoporous Mater*, 197: 244–251. http://dx.doi.org/10.1016/j.micromeso.2014.06.018

63. Hoppe A, Guldal N S, Boccaccini A R, 2011, A review of the biological response to ionic dissolution products from bioactive glasses and glass-ceramics. *Biomaterials*, 32(11): 2757–2774. http://dx.doi.org/10.1016/j.biomaterials.2011.01.004

64. Yamniuk A P, Vogel H J, 2005, Calcium- and magnesium-dependent interactions between calcium- and integrin-binding protein and the integrin αIIb cytoplasmic domain. *Protein Sci*, 14(6): 1429–1437. http://dx.doi.org/10.1110/ps.041312805

65. Zreiqat H, Howlett C, Zannettino A, *et al*., 2002, Mechanisms of magnesium-stimulated adhesion of osteoblastic cells to commonly used orthopaedic implants. *J Biomed Mater Res A*, 62(2): 175–184. http://dx.doi.org/10.1002/jbm.10270

66. Bouvard D, Pouwels J, De Franceschi N, *et al*., 2013, Integrin inactivators: Balancing cellular functions *in vitro* and *in vivo*. *Nat Rev Mol Cell Biol*, 14(7): 430–442. http://dx.doi.org/10.1038/nrm3599

67. Bourboulia D, Stetler-Stevenson W G, 2010, Matrix metalloproteinases (MMPs) and tissue inhibitors of metalloproteinases (TIMPs): Positive and negative regulators in tumor cell adhesion. *Semin Cancer Biol*, 20(3): 161–168. http://dx.doi.org/10.1016/j.semcancer.2010.05.002